Effects of Ag doping on LaMnO$_3$ photocatalysts for photoelectrochemical water splitting

Mohamed S. Afify[1] · Mohamed M. El Faham[1,4] · Usama Eldemerdash[1,3] · S. I. El-Dek[2] · Waleed M. A. El Rouby[2]

Abstract

As a redox material, perovskite is considered one of the most efficient photovoltaic materials for producing hydrogen via water splitting reactions. This study used a wet chemical method to synthesize La$_{1-x}$Ag$_x$MnO$_3$ nanoparticles ($0.00 \le x \le 0.09$). The formation, chemical composition, and morphology of samples were examined by field emission scanning electron microscopy (FE-SEM), X-ray diffraction (XRD), energy dispersive X-ray spectroscopy (EDX), and high-resolution transmission electron microscopy (HR-TEM). The optical properties were examined by ultraviolet visible (UV) diffuse reflectance spectroscopy. XRD demonstrated that the samples had a rhombohedral hexagonal structure with a space group R $\overline{3}$ c. The pore volume, pore size, and surface area were calculated and examined. The prepared samples were used as a photoanode in alkaline media for water splitting, and the photocurrent was measured. The photocurrent density recorded (14.01, 12.02, 11.67, and 10.28 µA/cm^2) for x = (0.09, 0.06, 0.03, and 0.00) at 1 V vs. Ag/AgCl, respectively. The smaller impedance of the sample ($x = 0.09$) photoanodes than the sample ($x = 0.00$), which displayed a considerable decrease in charge transfer resistance. The electron lifetime (τ) increased with increasing Ag concentration, where $x = 0.09$ has the largest electron lifetime (τ) = 10.04 ms. Therefore, the electron–hole recombination rate of La$_{0.91}$Ag$_{0.09}$MnO$_3$ is lower than LaMnO$_3$. The samples demonstrated long-term stability for 1 h and enhanced photoelectrochemical performance.

Keywords Nanoparticles · Manganites · Ag doping · Perovskite · Water splitting · Impedance spectroscopy

1 Introduction

The demand for clean, inexpensive, safe, and renewable energy sources has significantly increased over the last few years [1]. Accordingly, researchers have focused on obtaining energy from sunlight, which is a renewable and readily available source. Hydrogen is one of the most important forms of energy available; it can be obtained from sunlight and water [2–4].

One of the most important technologies for hydrogen production is photocatalytic hydrogen production from water, known as photoelectrochemical (PEC) water splitting. This process is a preferred solution because it is environmentally clean and economical for chemical fuels [5, 6]. Consequently, multiple techniques to increase hydrogen production by PEC have been examined [7–9].

PEC water splitting comprises three main stages: absorption of light, separation of charges, and surface chemical reaction and transportation. Metal oxides are commonly used in water splitting because of their photocorrosion resistance when in contact with an aqueous electrolyte. TiO$_2$ can be used as a photoanode for water splitting owing to its optical absorption and low cost [10–14]. However, its large bandgap (3.2 eV) limits its light absorption to the ultraviolet (UV) region, which represents only 4% of the incoming solar light [15, 16]. Therefore, a semiconductor with a narrower bandgap and good electron–hole separation is preferable for solar harvesting.

Perovskite semiconductors (ABO$_3$) are one of the most effective photovoltaic materials for hydrogen production via a water-splitting reaction owing to their thermal stability, adaptability, low cost, and broad bandgap (1.5–3.0 eV) [17, 18]. Lervolino et al. [19] synthesized n-type LaFeO$_3$ powder for hydrogen production via a PEC water-splitting reaction

✉ S. I. El-Dek
didi5550000@gmail.com

1   Basic Engineering Sciences Department, Benha Faculty of Engineering, Benha University, Benha, Egypt

2   Materials Science and Nanotechnology Department, Faculty of Postgraduate Studies for Advanced Sciences (PSAS), Beni-Suef University, Beni-Suef 62511, Egypt

3   Chemical & Petrochemical Engineering, Egypt Japan University of Science and Technology (EJUST), Alexandria, Egypt

4   Pyramids higher institute for Engineering and technology, Giza, Egypt

under UV-LED radiation using the solution combustion synthesis method. Pan et al. [20] reported that the photocurrent density of several n-type perovskite oxides ($LaNO_3$, $LaCrO_3$, $LaFeO_3$, and $LaMnO_3$) was 0.54 mA/cm^2. Recently, novel p-type perovskite semiconductors were used for PEC water splitting [21]. Maeda et al. [22] used a stable p-type semiconductor Rhodium-doped barium titanate ($BaTiO_3$:Rh) photocatalyst for water splitting and hydrogen production.

From specialized investigations, Ag can substitute for La ions. The ionic radii of Ag^+ and La^{3+} in 12-coordination are 1.22 and 1.36 Å, respectively [23]. The structural, magnetic, and electrical properties of doped MnO_3 manganese oxides have attracted attention for a range of applications. Ag can be used as an electrode material because it is stable in alkaline solutions, and it increases the electrical conductivity of the composite [24]. Perovskites have been synthesized using various processes, including solid phase, carbonate co-precipitation, and sol–gel methods. In comparison, a wet chemical method allows control of the kinetics and thermodynamic parameters during the reaction. This will helped to take control over the size and shape of the produced nanoparticles.

Based on the best of our knowledge, no one reported the photoelectrocatalytic properties of $La_{1-x}Ag_xMnO_3$ in alkaline medium.

In this study, $LaMnO_3$ has been prepared and used as photoanode material for oxygen evolution reaction and the effect of Ag doping on its properties and photoelectrocatalytic activity has been addressed.

2 Materials and methods

2.1 Materials

The following chemicals were utilized in this study: lanthanum (III) nitrate hexahydrate 99.99% (($La(NO_3)_3$·$6H_2O$, Sigma–Aldrich, Germany), stearic acid ($C_{18}H_{36}O_2$, Sigma–Aldrich, Germany), silver nitrate ($AgNO_3$, Sigma–Aldrich, Germany), Nafion (Sigma–Aldrich, Germany), manganese(II) nitrate tetrahydrate ($Mn(NO_3)_2$·$4H_2O$, Loba company, India) and ethanol (C_2H_5OH, VWR chemicals, EU). All chemicals were of analytical grade and used as received.

2.2 Synthesis of perovskite nanomaterials

The nanoparticle polycrystalline perovskite compounds [$La_{1-x}Ag_xMnO_3$] ($0.00 \leq x \leq 0.09$) were synthesized using a wet chemical method [25]. Lanthanum (III) nitrate hexahydrate, manganese (II) nitrate tetrahydrate, and silver nitrate were dissolved separately in 20 ml of bi-distilled water according to the stoichiometric ratio and then mixed. Molten

stearic acid (0.4 mol) was added to the mixture. Stirring continued until a black, uniform mixture had formed. The resulting mixture was heated to 120 ℃ in an oven for 3 h. The output materials were cooled to room temperature and heated again in an oven at 400 ℃ for 12 h to obtain the dried gel. The gel was then calcined at 800 ℃ for 2 h [26]. The resulting powders were ground and washed with a water/ethanol mixture (2:1) because they were not in a single phase according to XRD. Subsequently, the specimens were dried at 100 °C for 1 h and calcined at 950 ℃ for 3 h to obtain the $La_{1-x}Ag_xMnO_3$ nanoparticles. The samples from the synthesis process were labeled $x = 0.00$, $x = 0.03$, $x = 0.06$, and $x = 0.09$.

2.3 Characterization of the prepared materials

The crystallinity and phases identification of obtained samples were characterized by X-ray diffraction (XRD, PANalytical Empyrean, Netherlands) using CuKα radiation ($\lambda = 1.54060$ Å) at an accelerating voltage and current of 35 kV and 30 mA, respectively. The scan range was 5° to 80° at a scan step of 0.04°, with 0.5 s per step. The morphologies of prepared samples were analyzed by high-resolution transmission electron microscopy (HR-TEM, JEM-2100, JEOL, Japan) at an acceleration voltage of 200 kV. Field-emission scanning electron microscopy (FE-SEM, ZEISS Sigma HD, Germany) was performed at acceleration voltages of 1–3 kV in high vacuum mode to characterize the morphology of prepared samples. Elemental analysis was performed by energy-dispersive X-ray spectroscopy (EDX, SAMx IDfix, France) mounted on the SEM with an acceleration voltage of 15 kV. Brunauer–Emmett–Teller (BET, Quantachrome V- 1.21, USA) analysis was performed to determine the pore
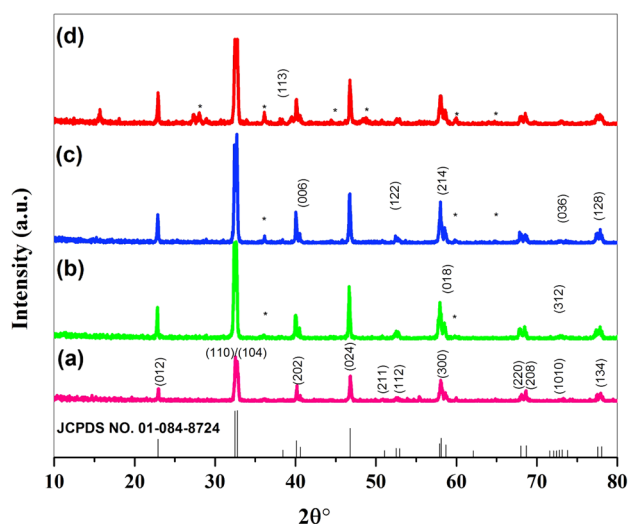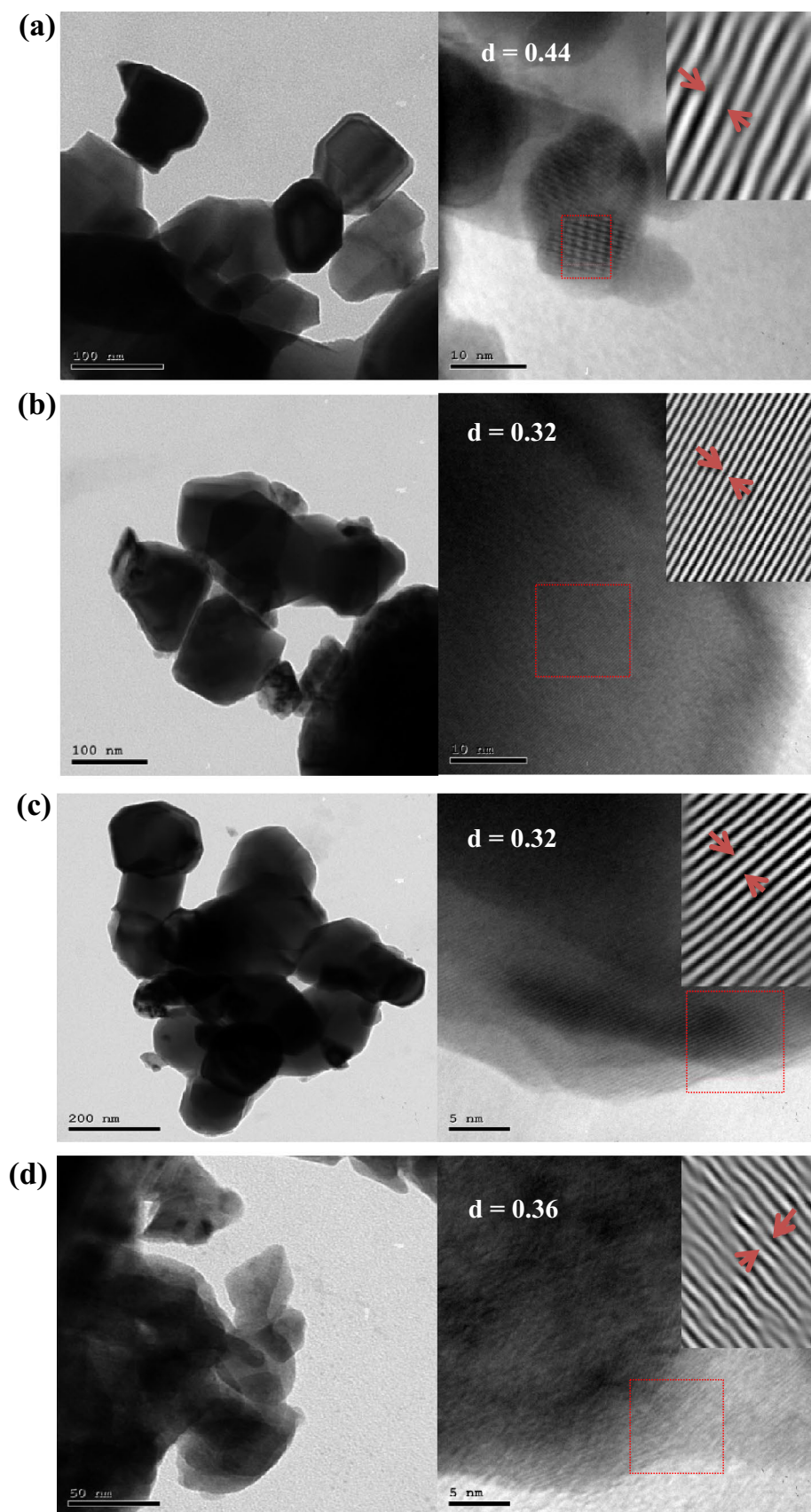

Fig. 1 XRD pattern of $La_{1-x}Ag_xMnO_3$ manganite *Mn_3O_4

Fig. 2 HR-TEM micrographs of La$_{1-x}$Ag$_x$MnO$_3$ manganite. **a** $x=0.00$ **b** $x=0.03$ **c** $x=0.06$ **d** $x=0.09$

volume, pore size distribution, and the surface area. The ultraviolet–visible (UV- vis) diffused reflectance spectra (DRS) were obtained from ultraviolet–visible spectrometer (Jasco V-750, USA) spectral range from 190 to 1800 nm.

2.4 Electrode preparation

The working electrodes were prepared by mixing 2.0 mg of the prepared powder ($x = 0.00$, $x = 0.03$, $x = 0.06$, and $x = 0.09$) with 400 μL of ethanol and 10 μL of Nafion solution (5 wt. %), at room temperature and the mixtures were sonicated for 30 min. Subsequently, 30 μL of the sonicated suspension was pipetted out (5 μL) every time and dripped onto a fluorine-doped tin oxide (FTO) surface (1 cm²) where it was allowed to dry for 30 min at 80 °C before use.

2.5 Photoelectrochemical study

An Autolab potentiostat (PGSTAT302 N) was employed to record all photoelectrochemical measurements, which included a three-electrode cell comprising a working electrode ($x = 0.00$, $x = 0.03$, $x = 0.06$, and $x = 0.09$) on the FTO surface, Ag/AgCl as the reference electrode, and platinum wire (Pt) as a counter electrode. All electrodes were submerged in a 0.5 M NaSO₄ electrolyte (pH = ~6.5) in a Teflon

photoelectrochemical cell and matched with a window for illumination. The photocurrent–potential curves were obtained by fluctuating the applied potential from (− 0.6 to 1 V) vs. Ag/AgCl electrode under illumination and dark circumstances. Solar simulation was achieved with a 150 W Xenon lamp paired with an air mass 1.5 global filter (Newport, USA) on a 1 cm² area of the working electrode. The simulator intensity was adjusted to one sun (100 mWcm^{-2}) using a digitalized portable energy meter console (Thorlabs, PM100D, USA) linked with a highly sensitive calibrated thermometer (Thorlabs, S310C, USA). Electrochemical impedance spectroscopy (EIS) was carried out at 0.9 V vs. Ag/AgCl over the frequency range, 0.05 Hz to 120 kHz, with an amplitude of 10 mV.

3 Results and discussion

3.1 Structural analysis

XRD revealed the patterns of the Ag- doped LaMnO₃ (La$_{1-x}$Ag$_x$MnO₃), as shown in Fig. 1, where ($0.00 \leq x \leq 0.09$). All sharp XRD peaks of samples were observed between 22.94° and 77.97°. The samples crystallized in a homogeneous/hexagonal structure according to the standard card of
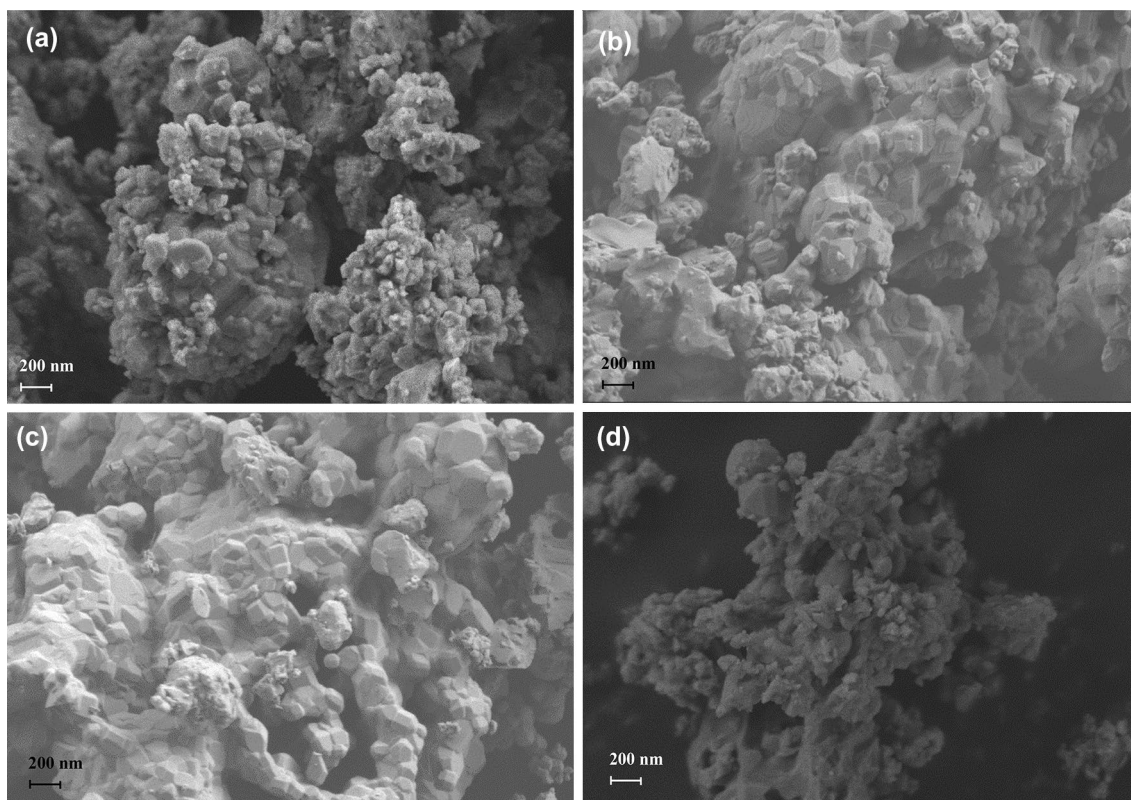

Fig. 3 FE-SEM micrographs for La$_{1-x}$Ag$_x$MnO₃ manganite. **a** $x = 0.00$ **b** $x = 0.03$ **c** $x = 0.06$ **d** $x = 0.09$

$La_{0.85}Ag_{0.15}MnO_3$ (JCPDS NO. 01–084-8724). Secondary phases of manganese oxides (Mn_3O_4) were indicated by the relevant small peaks. The perovskite lattice has a solubility limit for Ag with a large ionic radius. The experimental results from this investigation agree with previous reports [25, 27–31]. Based on the Scherrer equation [32], the average crystallite sizes were 54.6, 51.2, 59.5, and 42.8 nm for $x = 0.00$, 0.03, 0.06, and 0.09, respectively. XRD demonstrated that with increasing Ag doping, certain XRD peaks for the $LaMnO_3$ matrix broadened, indicating the nanocrystalline structure of the synthesized nano samples. The lattice parameters, unit cell volume, theoretical density, and tolerance factor are reported [25]. The previously mentioned variables for the samples were relatively constant, reflecting the stability of the layered structure. However, slight alterations were noted because of the limited amount of Ag. We expected that for large (Ag content), large peaks for a secondary phase will appear, indicating non-stoichiometric perovskite.

3.2 Morphological characterization

Figures 2 and 3 show the HRTEM and FESEM images of $La_{1-x}Ag_xMnO_3$ nanoparticles, respectively. The large particles had a geometric form with sharp edges (Fig. 2). However, a closer look revealed the hexagonal symmetry, which is in good correlation with the analysis of X-ray data as the manganite adopted the R $\overline{3}$ c space group as a part of the rhombohedral–hexagonal crystal symmetry. The four different samples had the same distribution and shape with extraordinary crystallinity of the particles at nano size. Certain agglomeration may be obtained from the shortage of surfactant combined with the high-temperature annealing. The particle size variation was attributed to the difference in the ionic radii of Ag^+ and La^{3+} on the equivalent lattice sites. The size decreased with increase in Ag content because of a small concentration of Mn_3O_4 secondary phase on the grain boundaries.

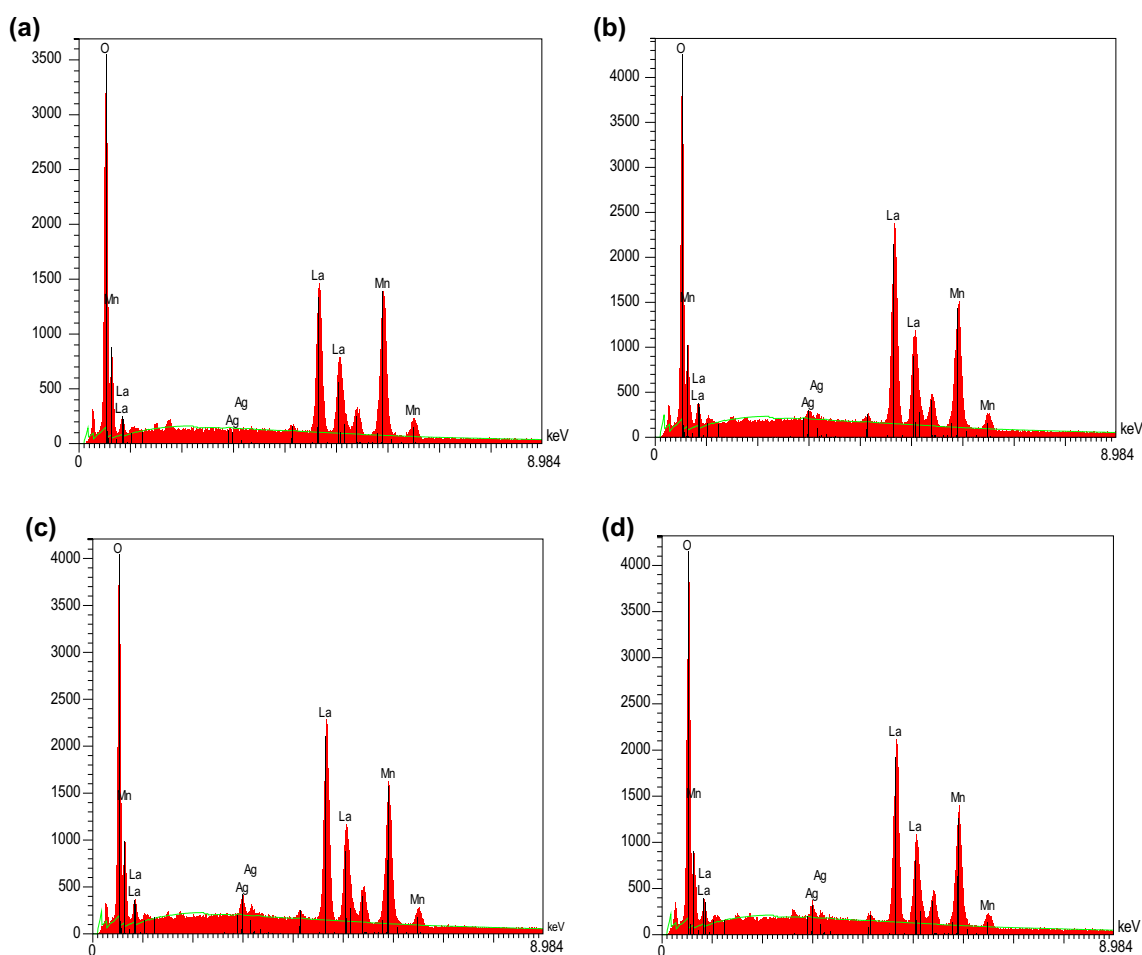FESEM demonstrated that the grains were stacked with clear boundaries (Fig. 3). The major observation was the

Fig. 4 EDX spectrum of $La_{1-x}Ag_xMnO_3$ manganite. **a** $x = 0.00$ **b** $x = 0.03$ **c** $x = 0.06$ **d** $x = 0.09$

hexagonal features, which provide evidence of the layered pattern of perovskite. As the Ag content was increased, additional compactness and the formation of layers were observed along with a small amount of impurities on the grain boundaries because the secondary phase diffused out of the grains via the pinning diffusion mechanism. The existence of all elements in prepared samples $La_{1-x}Ag_xMnO_3$ (x = 0.00, 0.03, 0.06, and 0.09) was investigated by EDX, as shown in Fig. 4. All elements (La, Ag, Mn, and O) were present without losses during annealing, highlighting the quality of the synthesis process.

3.3 Surface area measurements

Figure 5a shows the N_2-adsorption–desorption isotherms of $La_{1-x}Ag_xMnO_3$ nanoparticles. All the samples showed type IV isotherms with an H3-hysteresis loop, demonstrating mesoporous structures with regular pores (2–50 nm) [33, 34]. The specific surface areas of the samples were calculated using the BET theory. The average pore radius and total pore volumes were obtained using the Barrett–Joyner–Halenda (BJH) equation, as listed in Table 1. The average pore radius, specific surface area, and pore volume were affected by the Ag molar ratio. The largest surface area was observed for x = 0.03, but the pore radius was relatively unchanged. Hence, Ag was a good choice for tailoring the surface properties of perovskite.

The non-uniform changes in the surface area and pore volume with the Ag content were acceptable for the samples annealed at 950 ℃ because a high-density ceramic with magnetic properties was obtained. Moreover, a small amount of secondary phase was always present on the grain boundaries, which helped blocking some surface pores.

Figure 5b shows the pore size distribution for all samples, with the half pore radius ranging from 2.5 to 19 nm, demonstrating hierarchical porous structures, which have been shown to play a vital role in improving the photochemical characteristics by enhancing electron and ion transport [20]. A highly porous nanostructure can provide a large space for electrolyte transport in the electrode material, allowing the efficient use of electro-active materials and achieving high electrochemical performance [35].

3.4 Optical properties

The optical properties of prepared samples were characterized by UV–vis (DRS), as shown in Fig. 6. The Kubelka–Munk method was used to examine the optical properties [36]. The Kubelka–Munk equation for any wavelength is represented by Eq. 1.
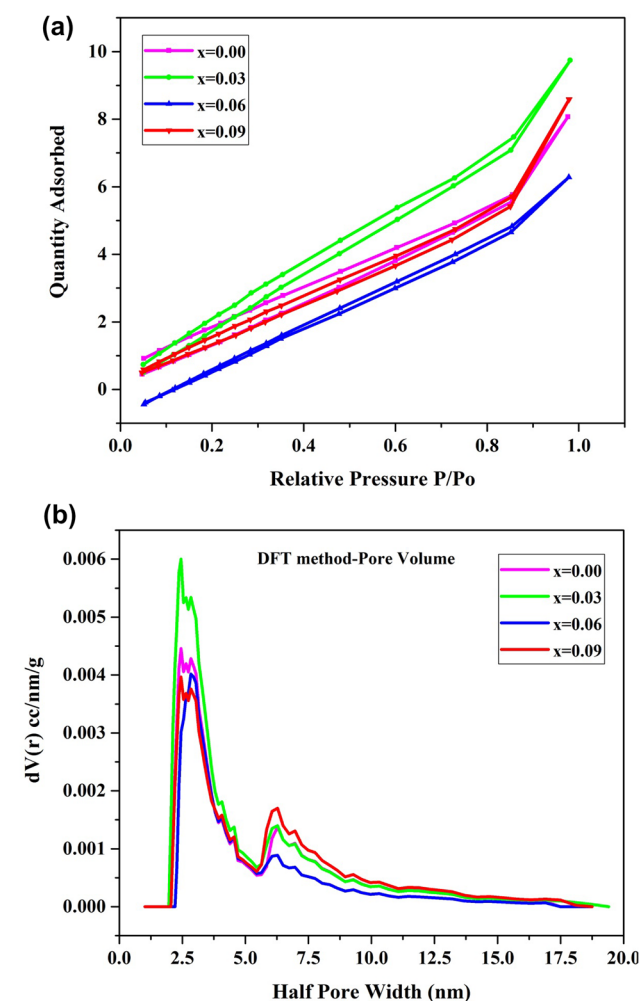
Fig. 5 a N_2 adsorption–desorption isotherms of $La_{1-x}Ag_xMnO_3$ manganite. **b** Pore size distributions for $La_{1-x}Ag_xMnO_3$ manganite

Table 1 The values of Surface area, Average pore radius and Total pore volumes for $La_{1-x}Ag_xMnO_3$ manganite samples

x	S_{BET} (m^2/g)	Average pore radius (nm)	Total pore volume (cm^3/g)
0.00	5.70	1.685	0.012
0.03	7.53	1.68	0.014
0.06	3.23	2.26	0.008
0.09	5.64	1.675	0.013

$$F(R) = \frac{(1-R)^2}{2R} \tag{1}$$

where F(R) is Kubelka–Munk function, and (R) is the absolute reflectance of the compounds. A high absorption peak was detected for all samples around ~280 nm, indicating that the most extreme absorption edge is in the ultraviolet region
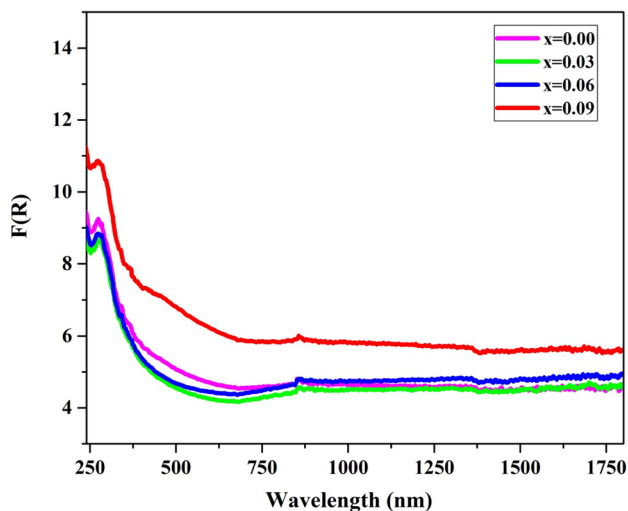
Fig. 6 Diffuse reflectance spectra of $La_{1-x}Ag_xMnO_3$ manganite in the IR-vis region at room temperature

[26]. This could be due to the charge transfer interaction between O^{2-} (2p) and Mn^{3+}(3d). The optical band gap (E_g) of all samples was calculated using Tauc's plot of $(F(R)h\nu)^2$ vs. $(h\nu)$ and an extrapolation of the linear sections of the curve to the energy axis using the equation below [26, 37, 38]:

$$[F(R)h\upsilon]^n = A(h\upsilon - E_g) \tag{2}$$

where $(h\upsilon)$ is the energy of a photon, (n) is a constant related to different types of electronic transitions, and (A) is an energy independent constant. Herein, the value of (n) is a clear evaluation of the transition type: $n = 1/2$ indicates a direct transition; $n = 2$ indicates an indirect transition; $n = 3/2$ denotes a direct forbidden transition; $n = 3$ is for an indirect forbidden transition. Figure 7 shows the Tauc's plot of the sample. The optical bandgaps for $x = 0.00$, 0.03, 0.06, and 0.09 were 2.670, 2.664, 2.661, and 2.660 eV, respectively. The optical band gap decreased with increase in Ag dopant concentration. The interaction between LaMnO₃ and Ag nanoparticles is primarily responsible for the change in bandgap. The Ag nanoparticles produced the
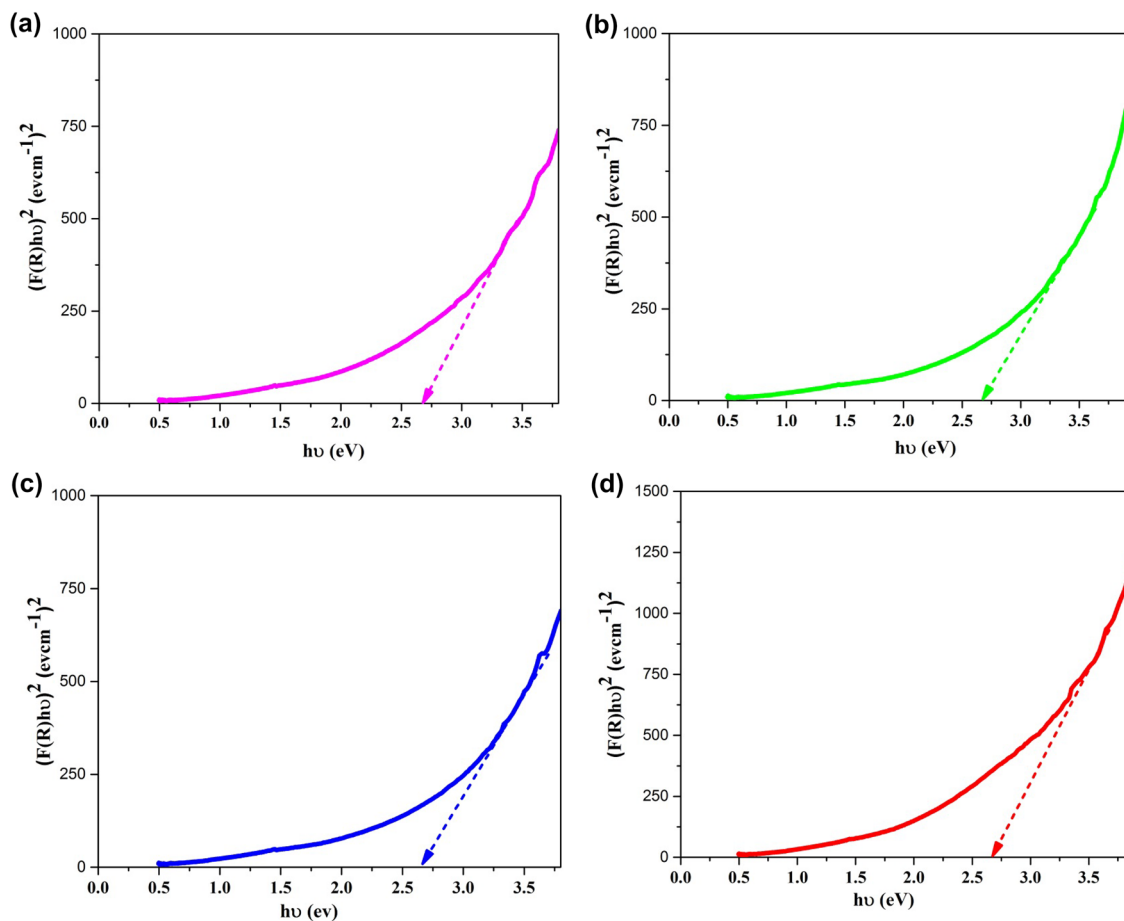

Fig. 7 The plot of $(F(R)h\nu)^2$ vs. photon energy $(h\nu)$ of $La_{1-x}Ag_xMnO_3$ manganite. **a** $x = 0.00$ **b** $x = 0.03$ **c** $x = 0.06$ **d** $x = 0.09$

trap levels between the conduction and valence bands of $LaMnO_3$. This decrease indicates the enhancement in the electronic properties (high transport ability of electrons in the $La_{1-x}Ag_xMnO_3$ structure by the presence of silver). Thus, with decreasing the bandgap energy, a wide range of light can be absorbed by $La_{1-x}Ag_xMnO_3$. Moreover, Ag is a plasmonic nanomaterial and it has excellent absorbing capability for the light. Thus, the presence of Ag in $La_{1-x}Ag_xMnO_3$ improving the light absorption properties of $La_{1-x}Ag_xMnO_3$.

In the present case, $n = 2$, Ag-doped $LaMnO_3$ is characterized by an indirect allowed transition. Ag^+ is the key factor contributing to the Fermi level and its position between valence and conduction band. The optical band gap did not significantly change; only a slight decrease was observed. This was attributed primarily to the very low Ag content ($0.00 \leq x \leq 0.09$). The largest Ag concentration $x = 0.09$ will lead to La (0.91), which is only a small change in the A cation concentration. Another plausible explanation is that the samples were annealed at 950 °C, which is sufficient to obtain a high dense, compactness, lower porosity, and opacity.

3.5 PEC water splitting

Figure 8a shows the linear sweeps voltammograms (LSV) curves recorded under chopped light conditions for all samples, demonstrating a gradual increase in the photocurrent densities for $LaMnO_3$ after Ag doping. Pure $LaMnO_3$ exhibited a photocurrent density of 13 μA cm^{-2} at 1 V vs. SCE. After Ag addition, the current density gradually increased to the same potential because of the electron-accepting nature of Ag and its high conductivity that facilitates charge carrier transport [39]. Accordingly, the electron–hole recombination rate decreased. When the nanocomposite was doped with Ag = 0.06 and 0.09, the photocurrent density showed the highest enhancement up to 18.5 μA cm^{-2} at the same potential, which is $\approx 42.3\%$ higher than that of pure $LaMnO_3$. Compared to previously published perovskites [40], the photocurrent of Ag-doped $LaMnO_3$ was improved owing to the smaller bandgap. The photoelectrochemical activity and stability of the fabricated photoanodes were assessed by testing the materials under chopped light conditions at 1 V vs. SCE, as shown in Fig. 8b. An instantaneous photocurrent was generated when the light was turned on. All samples were highly responsive to light, as observed by the increase in current and instant decrease when the light is switched on and off, respectively [41]. The spikes at the beginning of illumination indicate that some of the photo-produced holes at the electrode surface are filled with photogenerated electrons from the conduction band before being transferred to the electrolyte and occupied with electrons of the electrolyte-reduced species [42, 43]. The results indicate that the photocurrent produced by ($x = 0.09$) was highest, agreeing with Fig. 8a. This enhancement could be attributed to the increased rate of photogenerated electron–hole separation and efficient visible light harvesting.

The electrochemical impedance spectroscopy (EIS) was measured to evaluate the recombination of charge carriers in the photoanode and the charge transfer kinetics. All measurements were conducted in an aqueous solution of 0.5 M Na_2SO_4 under illumination in the frequency range between 0.05 Hz and 120 kHz. Figure 9 shows the Bode phase diagrams and Nyquist plots for all the electrodes used. The Nyquist plot was used to evaluate the charge transfer resistance, as shown in Fig. 9a. The smaller impedance trend of the sample ($x = 0.09$) photoanodes than the sample ($x = 0.00$) was attributed to Ag doping, which displayed a considerable decrease in charge transfer resistance. A probable reason could be the initiation of a new conduction path in the highest
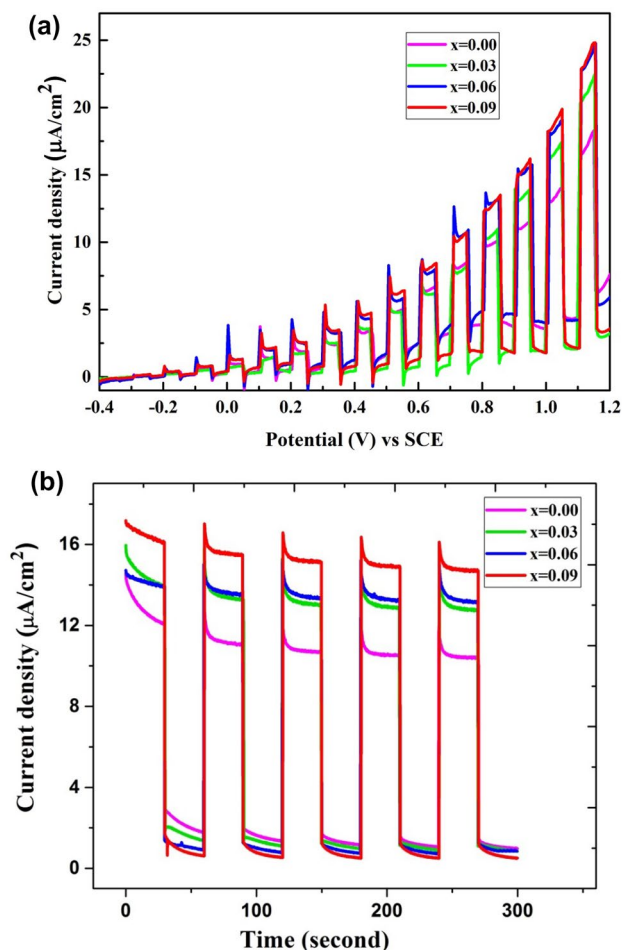

Fig. 8 **a** Linear sweep voltammograms of all prepared photoelectrodes. Light UV + Vis (ON–OFF) **b** Chronoamperometry (ON–OFF) Light UV + Vis

Ag ion content, either intragranular and/or intergranular. The primary conduction mechanism is valence exchange $Mn^{3+} \leftrightarrow Mn^{4+} + e^-$ because the Mn^{3+}/Mn^{4+} ratio was almost constant with increasing Ag in the perovskite lattice. Therefore, Ag^+ acts as a conductive network that interconnects the insulating grains of LaMnO$_3$.

Figure 9b shows the appropriate Bode phases of the utilized photoanodes. The electron lifetimes (τ) of the prepared samples used as photoelectrodes were determined based on the associated maximum frequency using the equation below [44, 45].

$$\tau = \frac{1}{(2\pi f_{peak})} \tag{4}$$

where f_{peak} is the maximum frequency of the characteristic peak in the mid-frequency range (0.05–120 kHz). The peak position appears to be a lower frequency with increasing Ag content. Table 2 list the values of electron lifetimes (τ) and
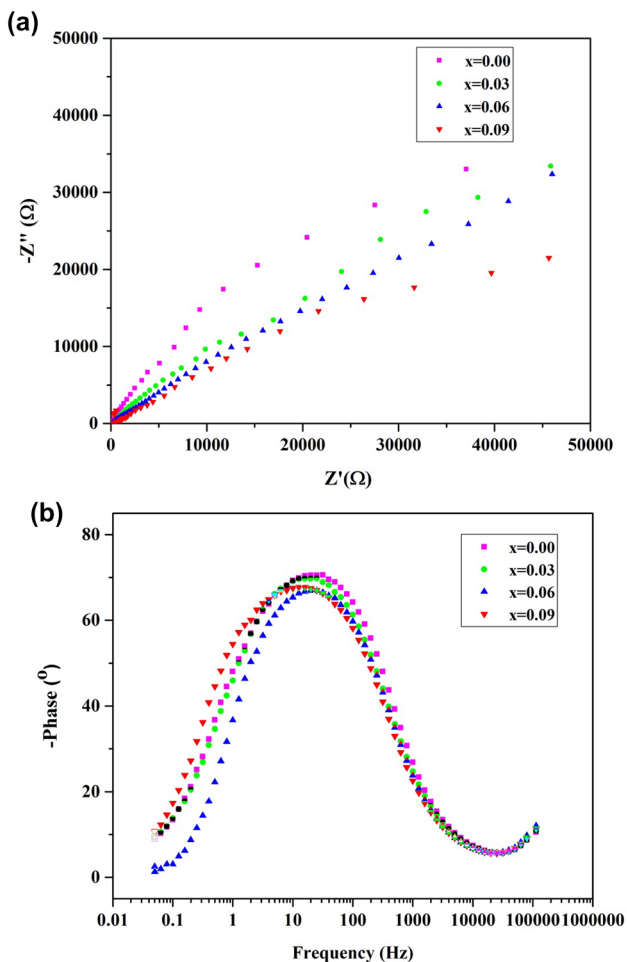
Table 2 EIS fitted electrochemical parameters of photoelectrodes consisted of La$_{1-x}$Ag$_x$MnO$_3$ manganite samples

x	f_{peak} (Hz)	(FWMH)	τ (ms)
0.00	31.60	486.38	5.03
0.03	25.11	401.82	6.33
0.06	19.95	354.14	7.97
0.09	15.84	479.25	10.04

the full width at half maximum (FWHM), which were calculated from the peak broadening at full maximum for each sample. The electron lifetime (τ) increased with increasing Ag concentration, where $x = 0.09$ has the largest electron lifetime (τ) = 10.04 ms. Therefore, the electron–hole recombination rate of La$_{0.91}$Ag$_{0.09}$MnO$_3$ is lower than LaMnO$_3$. The contribution of the current in manganites is related to multiple factors. The first is the intensity of incident light, number of charge carriers, and their type and mobility. Another plausible explanation could be the probable existence of oxygen vacancies generated during the annealing process. These vacancies act as trapping centers for the electrons generated from Mn^{3+} and Mn^{4+} ions.

Chronoamperometric measurements were used to determine the photocurrent stability of all photoanodes at 1 V vs. Ag/AgCl in a 0.5 M Na$_2$SO$_4$ electrolyte under constant illumination of one synthetic sun (one sun) for 1 h. Figure 10 shows all the photoanodes samples exhibited an obvious long-term stability for 1 h. This demonstrated that La$_{1-x}$Ag$_x$MnO$_3$ photoanode was chemically stable under these experimental circumstances. The photocurrent density recorded (14.01, 12.02, 11.67, and 10.28 µA/cm^2) for $x = (0.09, 0.06, 0.03,$ and 0.00), respectively. The increase in photocurrent was almost 36.3%, corresponding

Fig. 9 **a** Nyquist and **b** Bode (phase angle versus frequency) diagrams of the EIS data obtained for the $x = 0.00, 0.03, 0.06, 0.09$ photoelectrodes at 1VAg/AgCl in 0.5 M NaSO$_4$ under illumination
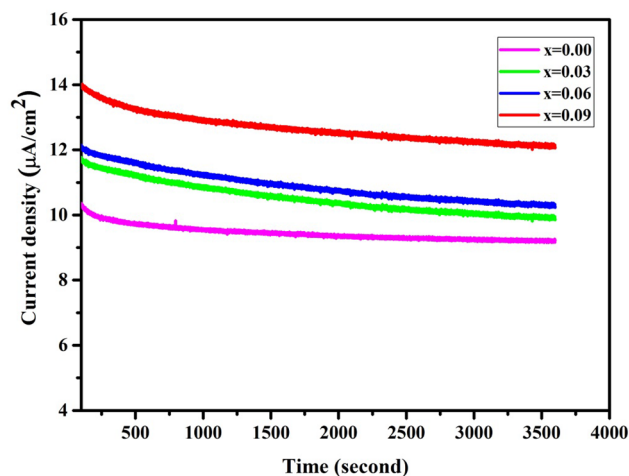
Fig. 10 Stability tests at 1.0 V/SCE

Table 3 Comparison with reported literature

Sample	Crystal Size (nm)	Surface area (m^2/g)	Photocurrent density	Ref
$LaMnO_3$ film at the external potential $+0.5$ V	45.44	6.9	0.27 mA/cm^2	[20]
$LaMn_{1-x}Cu_xO_3$ films at the external potential -0.5 V	31.56	14	0.41 mA/cm^2	[39]
$La_{0.91}Ag_{0.09}MnO_3$ powder	42.8	5.64	0.14 mA/cm^2	Our work

to 0.09 wt. % of Ag. Maybe 1 h as a stability test is just an indicator for the stability of the electrode materials but, in our next study we will prolong the stability test for 24 or even 100 h in order to sand on the real stability of the photoanode material.

The comparison with reported literature was carried out (the crystal size, surface area, and photocurrent density) in Table 3.

4 Conclusion

The straightforward synthesis of Ag-doped $LaMnO_3$ with a perovskite structure was performed. The samples belong to the rhombohedral/hexagonal crystal symmetry. All samples demonstrated excellent crystallinity, regardless of their doping ratio and despite the small crystallite size. The pore size for all samples was < 3 nm, indicating mesoporous nature of the structures. The increase in Ag doping content resulted in the monotonic narrowing of the optical bandgap. The photocurrent density increased by 36.3% with 0.09 wt. % Ag doping compared to the undoped parent $LaMnO_3$. All samples demonstrated long-term stability for 1 h. A longer lifetime of 10.04 ms was recorded for the largest Ag content. Nevertheless, further investigations of different metallic dopants in $LaMnO_3$ with versatile morphologies will be required.

Author contributions El-D: designed the experiments, supervise all the work and contributed to the discussion of the results. ElR: contributed in the sample electrochemical measurements supervise the whole work and contribute the discussion. A: was responsible of the sample preparation, measurements, figures plotting and discussion of the results. E and el F: were supervising the whole work, writing the draft manuscript.

All authors contribute to the revisions of the manuscript in its final form and agree to the submission.

Declarations

Conflict of interest The authors declare that they have no conflict of interest.

Ethics approval and consent to participate All authors approved the submission.

Consent for publication All authors approved the submission.

References

1. S. Chu, A. Majumdar, Opport Chall Sustain Energy Future (2012). https://doi.org/10.1038/nature11475
2. C. Jiang, S.J.A. Moniz, A. Wang, T. Zhang, J. Tang, Chem Soc Rev splitting—materials and challenges. Chem. Soc. Rev. **46**, 4645–4660 (2017). https://doi.org/10.1039/C6CS00306K
3. S.Y. Tee, K.Y. Win, W.S. Teo, L. Koh, S. Liu, C.P. Teng, Recent Prog Energy-Driv Water Split (2017). https://doi.org/10.1002/advs.201600337
4. H. Ahmad, S.K. Kamarudin, L.J. Minggu, M. Kassim, Hydrogen from photocatalytic water splitting process : a review. Renew. Sustain. Energy Rev. **43**, 599–610 (2015). https://doi.org/10.1016/j.rser.2014.10.101
5. L. Liu, Z. Liu, A. Liu, X. Gu, C. Ge, F. Gao, Engineering the TiO_2—graphene interface to enhance photocatalytic H$_2$

production. Chemsuschem (2014). https://doi.org/10.1002/cssc.201300941

6. M.Z. Jacobson, Clean Air Improv Health Hydro Fuel-Cell Vehicles. (2014). https://doi.org/10.1126/science.1109157

7. A. Esmail, A. Bakr, W.M.A. El, M.D. Khan, A.A. Farghali, B. Xulu, Synthesis and characterization of Z-scheme α -Fe$_2$O$_3$ NTs / ruptured tubular g-C$_3$N$_4$ for enhanced photoelectrochemical water oxidation. Sol. Energy. **193**, 403–412 (2019). https://doi.org/10.1016/j.solener.2019.09.052

8. M. Dilshad, M. Aamir, M. Sohail, M. Sher, J. Akhtar, Novel single source precursor for synthesis of Sb$_2$Se$_3$ nanorods and deposition of thin films by AACVD : photo-electrochemical study for water reduction catalysis. Sol : Energy. **169**, 526–534 (2018). https://doi.org/10.1016/j.solener.2018.05.026

9. M. Dilshad, M. Aamir, M. Sohail, M. Sher, N. Baig, J. Akhtar, M. Azad, N. Revaprasadu, Bis (selenobenzoato) dibutyltin (IV) as a single source precursor for the synthesis of SnSe nanosheets and their photoelectrochemical study for water splitting. Dalton Trans. **47**, 5465–5473 (2018). https://doi.org/10.1039/C8DT00285A

10. L. Gao, Y. Li, J. Ren, S. Wang, R. Wang, G. Fu, Y. Hu, Passivation of defect states in anatase TiO$_2$ hollow spheres with Mg doping: realizing efficient photocatalytic overall water splitting. Appl. Catal. B Environ. **202**, 127–133 (2017)

11. N. Ahmed, A.A. Farghali, W.M.A. El Rouby, N.K. Allam, Enhanced photoelectrochemical water splitting characteristics of TiO$_2$ hollow porous spheres by embedding graphene as an electron transfer channel. Int. J. Hydrogen Energy **42**, 29131–29139 (2017)

12. R.A. Sayed, S.E. Abd El Hafiz, N. Gamal, Y. GadelHak, W.M.A. El Rouby, Co-Fe layered double hydroxide decorated titanate nanowires for overall photoelectrochemical water splitting. J. Alloys Compd. **728**, 1171–1179 (2017). https://doi.org/10.1016/j.jallcom.2017.09.083

13. M.H. Elbakkay, W.M.A. El Rouby, S.I. El-Dek, A.A. Farghali, S-TiO2/S-reduced graphene oxide for enhanced photoelectrochemical water splitting. Appl. Surf. Sci. **439**, 1088–1102 (2018). https://doi.org/10.1016/j.apsusc.2018.01.070

14. H. Li, W. Dong, J. Xi, G. Du, Z. Ji, 3D flowerlike TiO$_2$/GO and TiO$_2$/MoS$_2$ heterostructures with enhanced photoelectrochemical water splitting. J. Mater. Sci. (2018). https://doi.org/10.1007/s10853-018-2051-8

15. S.G. Kumar, L.G. Devi, Review on modified TiO2 photocatalysis under UV/visible light: selected results and related mechanisms on interfacial charge carrier transfer dynamics. J. Phys. Chem. A **115**, 13211–13241 (2011)

16. A.B. Murphy, P.R.F. Barnes, L.K. Randeniya, I.C. Plumb, I.E. Grey, M.D. Horne, J.A. Glasscock, Efficiency of solar water splitting using semiconductor electrodes. Int. J. Hydrogen Energy **31**, 1999–2017 (2006)

17. G. Zhang, G. Liu, J.T.S. Irvine, Chem Soc Rev inorganic perovskite photocatalysts for solar energy utilization. Chem. Soc. Rev. **45**, 5951–5984 (2016). https://doi.org/10.1039/C5CS00769K

18. M. Kubicek, H. Bork, J.L.M. Rupp, Class for solar-to-fuel conversion processes. J. Mater. Chem. A Mater. Energy Sustain. **5**, 11983–12000 (2017). https://doi.org/10.1039/C7TA00987A

19. G. Iervolino, V. Vaiano, D. Sannino, L. Rizzo, P. Ciambelli, Production of hydrogen from glucose by LaFeO$_3$ based photocatalytic process during water treatment. Int. J. Hydrogen Energy. **41**, 959–966 (2016). https://doi.org/10.1016/j.ijhydene.2015.10.085

20. G.-T. Pan, S. Chong, K.-L. Pan, M.-B. Chang, T.-C.-K. Yang, P. Shukla, The study of photoelectrochemical properties of LaMnO$_3$, LaFeO$_3$, LaCrO$_3$, and LaNiO$_3$ photoelectrodes for hydrogen production. Clean Technol Environ Policy (2017). https://doi.org/10.1007/s10098-016-1319-4

21. K. Iwashina, A. Kudo, Rh-doped SrTiO$_3$ photocatalyst electrode showing cathodic photocurrent for water splitting under visible-light irradiation. J. Am. Chem. Soc **133**, 13272–13275 (2011). https://doi.org/10.1021/ja2050315

22. K. Maeda, Rhodium-doped barium titanate perovskite as a stable p—type semiconductor photocatalyst for hydrogen evolution under visible light. ACS Appl. Mater. Interfaces **6**, 2167–2173 (2014). https://doi.org/10.1021/am405293e

23. R.D. Shanon, Revised effective ionic radii and systematic studies of interatomic distances in halides and chalcogenides. Acta Crystallogr Sect A. **32**, 751–767 (1976)

24. S. Enache, M. Dragan, M. Varlam, K. Petrov, Electronic percolation threshold of self- standing Ag-LaCoO$_3$ porous electrodes for practical applications. Materials. **12**, 2359–2360 (2019)

25. M.S. Afify, M.M. El Faham, U. Eldemerdash, W.M.A. El Rouby, S.I. El-Dek, Room temperature ferromagnetism in Ag doped LaMnO$_3$ nanoparticles. J. Alloys Compd. **861**, 158570 (2020). https://doi.org/10.1016/j.jallcom.2020.158570

26. M. Shaterian, M. Enhessari, D. Rabbani, M. Asghari, M. Salavati-Niasari, Synthesis, characterization and photocatalytic activity of LaMnO3 nanoparticles. Appl. Surf. Sci. **318**, 213–217 (2014). https://doi.org/10.1016/j.apsusc.2014.03.087

27. T. Tang, K.M. Gu, Q.Q. Cao, D.H. Wang, S.Y. Zhang, Y.W. Du, Magnetocaloric properties of Ag-substituted perovskite-type manganites. J. Magn. Magn. Mater. **222**, 110–114 (2000). https://doi.org/10.1016/S0304-8853(00)00544-8

28. C.O.E. Eromosele, B.I. Ita, A.E. Osoh, F.E.E. Eromosele, Low-temperature solution- combustion synthesis and magneto-structural characterization of polycrystalline La1−x AgyMnO$_3$ (y ≤ x) manganites. Int. J. Self-Propag. High-Temp. Synth. **1**(25), 23–29 (2016). https://doi.org/10.3103/S1061386216010040

29. Zhang S., Sun T., Ji F., Dong G., Liu Y., Li Z., Zhang H., Chen Q., Liu X. 2019 Electrical and magnetic properties of La1-Ag MnO3 (0 ≤ x ≤ 0. 5) polycrystalline ceramics by combination of first principles calculations and experimental methods. J. Alloy. Compd. 808:151709

30. S.L. Ye, W.H. Song, J.M. Dai, K.Y. Wang, S.G. Wang, C.L. Zhang, Effect of Ag substitution on the transport property and magnetoresistance of LaMnO3. J. Magn. Magn. Mater. **248**, 26–33 (2002). https://doi.org/10.1016/S0304-8853(02)00017-3

31. M.B. Bellakki, C. Shivakumara, N.Y. Vasanthacharya, A.S. Prakash, Rapid synthesis of room temperature ferromagnetic Ag-doped LaMnO$_3$ perovskite phases by the solution combustion method. Mater. Res. Bull. **45**, 1685–1691 (2010). https://doi.org/10.1016/j.materresbull.2010.06.063

32. B.D. Cullity, S.R. Stock, *Elements of X-Ray Diffraction* (Pearson Education, Limited, 2013)

33. J. Luo, X. Zhou, F. Yang, X. Ning, L. Zhan, Z. Wu, Generating a captivating S-scheme CuBi$_2$O$_4$ / CoV$_2$O$_6$ heterojunction with boosted charge spatial separation for efficiently removing tetracycline antibiotic from wastewater Generating a captivating S-scheme CuBi$_2$O$_4$ / CoV$_2$O$_6$ heterojunction with boosted charge spatial separation for efficiently removing tetracycline antibiotic from wastewater. J. Clean. Prod. **357**, 131992 (2022). https://doi.org/10.1016/j.jclepro.2022.131992

34. J. Luo, J. Chen, X. Chen, X. Ning, L. Zhan, X. Zhou, Construction of cerium oxide nanoparticles immobilized on the surface of zinc vanadate nanoflowers for accelerated photocatalytic degradation of tetracycline under visible light irradiation. J. Colloid Interface Sci. **587**, 831–844 (2020). https://doi.org/10.1016/j.jcis.2020.11.044

35. Y. Tsai, W. Yang, K. Lee, C. Huang, An effective electrodeposition mode for porous MnO$_2$/Ni foam composite for asymmetric supercapacitors. Materials (2016). https://doi.org/10.3390/ma9040246

36. P. Kubelka, F.Z. Munk, Tech. Phys. **12**, 593–601 (1931)

37. E. Szabo-Bardos, K. Somogyi, N. Toro, G. Kiss, A. Horvath, Photocatalytic decomposition of l-phenylalanine over TiO$_2$:

Identification of intermediates and the mechanism of photodegradation. Appl. Catal. B Environ. **101**, 471–478 (2011). https://doi.org/10.1016/j.apcatb.2010.10.018

38. A.S. Patra, N.V. Kumar, D. Barpuzary, M. De, M. Qureshi, Strontium doped lanthanum manganites for efficient and robust photocatalytic water oxidation coupled with graphene oxide. Mater. Lett. **131**, 125–127 (2014). https://doi.org/10.1016/j.matlet.2014.05.176

39. P. Sfirloaga, G. Vlase, T. Vlase, I. Malaescu, C.N. Marin, P. Vlazan, Silver doping in lanthanum manganite materials: structural and electrical properties. J. Therm. Anal. Calorim. **142**, 1817–1823 (2020). https://doi.org/10.1007/s10973-020-10095-1

40. Hk. ElEmam, S.I. El-Dek, W.M.A. ElRouby, Aerosol spray assisted synthesis of Ni-doped BaTiO 3 hollow porous spheres/graphene as photoanode for water splitting. J. Electrochem. Soc. (2021). https://doi.org/10.1149/1945-7111/ac001e

41. G. Pan, S. Chong, T.C. Yang, P. Shukla, W. Siong, J. Ching, Results in physics effect of copper on the growth and photochemical properties of lanthanum manganite film electrode. Results Phys. **7**, 2118–2123 (2017). https://doi.org/10.1016/j.rinp.2017.06.011

42. D. Cao, Q. Wang, Z. Liu, H. Zhang, Y. Wang, R. Jin, S. Gao, Enhanced the photoelectrocatalytic performance of TiO$_2$ nanotube arrays by the synergistic sensitization of Ag–AgBr nanospheres. Spectro Acta Part A Mol. Biomol. Spectrosc. **227**, 117674 (2020). https://doi.org/10.1016/j.saa.2019.117674

43. X. Tian, Q. Wang, Q. Zhao, L. Qiu, X. Zhang, S. Gao, SILAR deposition of CuO nanosheets on the TiO$_2$ nanotube arrays for the high performance solar cells and photocatalysts. Sep. Purif. Technol. **209**, 368–374 (2019). https://doi.org/10.1016/j.seppur.2018.07.057

44. R. Kern, R. Sastrawan, J. Ferber, R. Stangl, J. Luther, Modeling and interpretation of electrical impedance spectra of dye solar cells operated under open-circuit conditions. Electrochim. Acta **47**, 4213–4225 (2002). https://doi.org/10.1016/S0013-4686(02)00444-9

45. A.I. Rafieh, P. Ekanayake, A.L. Tan, C.M. Lim, Effects of ionic radii of co-dopants (Mg, Ca, Al and La) in TiO$_2$ on performance of dye-sensitized solar cells. Sol. Energy **141**, 249–255 (2017). https://doi.org/10.1016/j.solener.2016.11.052